Advanced Powder Materials 4 (2025) 100284

Contents lists available at ScienceDirect

Advanced Powder Materials

journal homepage: www.keaipublishing.com/en/journals/advanced-powder-materials

Dual electric fields in Ni-CdS@Ni(OH)$_2$ heterojunction: A synergistic spatial charge separation approach for enhanced coupled CO_2 photoreduction and selective toluene oxidation

Khakemin Khan [a,1,*], Ahmed Mahmood Idris [b,1,***], Haseebul Hassan [c,1], Sajjad Haider [c], Salah Ud-Din Khan [d], Antonio Miotello [a,**], Ihsanullah Khan [a]

[a] Department of Physics, University of Trento, Via Sommarive 14, 38123, Trento, Italy
[b] Zhejiang Normal University School of Physics and Electronic Information Engineering, Jinhua 321004, China
[c] Chemical Engineering Department, College of Engineering, King Saud University, P.O. Box 800, Riyadh 11421, Saudi Arabia
[d] Sustainable Energy Technologies Center, College of Engineering, King Saud University, P.O. Box 800, Riyadh 11421, Saudi Arabia

ARTICLE INFO

Keywords:
Dual built-in electric fields
Spatial charge separation
Integrated redox reactions CO_2 reduction
Toluene oxidation
Semiconductor photocatalysis

ABSTRACT

Simultaneously inducing dual built-in electric fields (EFs) both within a single component and at the heterojunction interface creates a dual-driving force that is crucial for promoting spatial charge separation. This is particularly significant in challenging coupled systems, such as CO_2 photoreduction integrated with selective oxidation of toluene to benzaldehyde. However, developing such a system is quite challenging and often requires a precise design and engineering. Herein, we demonstrate a unique Ni-CdS@Ni(OH)$_2$ heterojunction synthesized via an *in-situ* self-assembly method. Comprehensive mechanistic and theoretical investigations reveal that the Ni-CdS@Ni(OH)$_2$ heterojunction induces dual electric fields (EFs): an intrinsic polarized electric-field within the CdS lattice from Ni doping and an interfacial electric-field from the growth of ultrathin nanosheets of Ni(OH)$_2$ on Ni-CdS nanorods, enabling efficient spatial charge separation and enhanced redox potential. As proof of concept, the Ni-CdS@Ni(OH)$_2$ heterojunction simultaneously exhibits outstanding bifunctional photocatalytic performance, producing CO at a rate of 427 μmol g^{-1} h^{-1} and selectively oxidizing toluene to benzaldehyde at a rate of 1476 μmol g^{-1} h^{-1} with a selectivity exceeding 85%. This work offers a promising strategy to optimize the utilization of photogenerated carriers in heterojunction photocatalysts, advancing synergistic photocatalytic redox systems.

1. Introduction

Photoreduction of carbon dioxide (CO_2) into valuable chemical feedstock and fuels using water as a proton source and electron donor through artificial photosynthesis is an emerging technique that addresses both energy and environmental challenges [1–3]. This process involves the use of photoexcited electrons to reduce CO_2 into gaseous or liquid carbonaceous products such as CO, CH_4, HCOOH, and CH_3OH, while photoexcited holes oxidize water to produce O_2. However, from a thermodynamic perspective, the photocatalytic water oxidation half-reaction is particularly challenging due to its sluggish four-electron transfer process, which significantly limits the overall system efficiency [2,4–6]. To overcome this limitation, non-polar sacrificial reagents such as ethyl acetate, triethanolamine, and isopropyl alcohol are often used as alternative electron donors instead of water to improve photoreduction efficiency. Nevertheless, the use of non-polar solvents imposes difficulties in identifying the carbon source of the resulting products, raising doubts about whether the observed yields are originated from photoreduction of CO_2 or solvent transformation. This also leads to the production of undesirable byproducts and affects reaction stability. Most critically, the use

* Corresponding author.
** Corresponding author.
*** Corresponding author.
E-mail addresses: khakemin.khan@unitn.it (K. Khan), ahmed503@zjnu.edu.cn (A.M. Idris), Haseebul.hassan@unitn.it (H. Hassan), shaider@ksu.edu.sa (S. Haider), drskhan@ksu.edu.sa (S.U.-D. Khan), antonio.miotello@unitn.it (A. Miotello), Ihsanullah.khan@unitn.it (I. Khan).
Peer review under the responsibility of Central South University.
[1] These authors have contributed equally to the work.

https://doi.org/10.1016/j.apmate.2025.100284
Received 13 February 2025; Received in revised form 13 March 2025; Accepted 16 March 2025
Available online 21 March 2025

of sacrificial reagents wastes the energy potential of photogenerated charges, limiting the conversion efficiency of solar-to-chemical energy [7,8].

To address these challenges, several sacrificial reagent-free CO_2 photoreduction systems have been proposed. However, these systems typically exhibit low conversion efficiency due to limited charge separation, absence of a proton source and low activation of CO_2 without sacrificial reagents. Considering these limitations, an integrated photoredox system has been proposed, which involves coupling the photoreduction of CO_2 or H_2 reaction with photooxidation of organic compounds in a single straight forward process, utilizing the full potential of photogenerated electrons and holes. This approach offers a mutually beneficial strategy, simultaneously producing valuable reduction and oxidation products without using any sacrificial reagents. In such a system, the photogenerated electrons are directly utilized to reduce CO_2, while organic compounds replace sacrificial agents and water by consuming the photogenerated holes to yield value-added organic chemicals. This scenario prevents the waste of photogenerated holes by water oxidation-half reaction and sacrificial reagents, significantly enhancing overall system efficiency [9–11]. However, developing such a system particularly for coupling CO_2 photoreduction with selective oxidation of toluene to BD is challenging and often requires precise design and engineering due to the thermodynamic and kinetic challenges associated with activating the inert C (sp^3)-H bond of toluene [12–14]. This reaction is important for synthesizing high-value oxygenated products and serves as an essential feedstock in industries such as pharmaceuticals, solvents, dyes, and perfumes. Therefore, the rational design of an effective, eco-friendly, cost-effective, and stable photocatalyst with a broad solar response, high conversion efficiency, straddling redox potentials to meet both kinetic and thermodynamic requirements of photoredox system is highly essential to achieving a high photocatalytic activity and selectivity.

Among the various semiconductor photocatalysts, metal chalcogenides, particularly CdS and its derivatives, have emerged as highly promising visible-light-responsive materials with significant reductive capabilities for diverse applications. Their growing prominence can be attributed to their optimal bandgaps, distinctive electronic structures, and tunable optical properties, all of which collectively enhance their performance in photocatalytic processes [15–17]. Despite their promise, the performance of pristine CdS is limited due to poor charge separation efficiency, severe charge recombination and susceptibility to photocorrosion under catalytic conditions. To address these challenges, forming CdS-based heterojunction through surface engineering is considered a promising strategy. This approach induces external IEF at the heterojunction interface, which serving as a driving force to significantly enhance the surface charge separation efficiency of pristine CdS [16, 18–20]. In this regard, recent investigations demonstrated that $Ni(OH)_2$ nanoparticles, particularly two-dimensional ultrathin nanosheets, can serve as efficient and cost-effective surface modifier to suppress charge recombination and promote surface charge separation and transfer for enhanced photocatalytic performance [21–23]. This is due to its unique porous ultrathin nanosheets offering significant advantages, such as large surface area that increases the number of catalytically active sites for redox reactions [24–26].

On the other hand, inducing IEF via doping foreign elements into the semiconductor lattice is regarded as an internal driving force for charge separation [27,28]. For example, it has been theoretically and experimentally proven that doping heteroatoms such as phosphorus (P), iron (Fe) and nitrogen (N) atoms into the lattice of CdS can alter its electronic structural properties, induce impurity states within the bandgap and create localized charge region due to different valence states between dopant and CdS [17,29,30]. This can result in piezoelectric effects in CdS, which has a wurtzite structure with inherent piezoelectric properties, thereby generating internal electric field [2,31–33]. To the best of our knowledge, strategies to enhance charge separation both within the bulk of CdS and at its surface, while increasing the availability of surface-active sites, remains elusive. Such a strategy could be realized by simultaneously inducing dual electric fields (EFs) through doping heteroatoms into the CdS lattice, alongside with the EF generated at the heterojunction interface. These combined mechanisms could serve as dual driving forces (DDFs) for spatial charge separation.

Herein, a unique nanostructure p-n heterojunction model of Ni-CdS@$Ni(OH)_2$ was precisely fabricated by growing a p-type $Ni(OH)_2$ porous ultrathin nanosheets on the surface of n-type Ni-CdS nanorods via the solvothermal *in-situ* assembly method. Comprehensive mechanistic and theoretical investigations revealed that the Ni-CdS@$Ni(OH)_2$ heterojunction incorporates dual IEFs: one within the CdS crystal lattice through Ni doping, and another at the interface between Ni-CdS and $Ni(OH)_2$, operating in a type II electron transfer mode. Besides, the unique architecture of Ni-CdS@$Ni(OH)_2$ heterojunction provides numerous surface-active sites, enhances light absorption through multiple scattering and facilitates the efficient transfer of photogenerated carriers at the heterojunction interface, as confirmed by various characterization techniques. Consequently, the Ni-CdS@$Ni(OH)_2$ exhibits superior bifunctional photocatalytic performance, achieving a CO with a production rate of 427 μmol g^{-1} h^{-1} and selectively oxidizing toluene to benzaldehyde at a rate of 1 476 μmol g^{-1} h^{-1} with a selectivity exceeding 85%. This study presents a simple and effective strategy for developing effective photocatalysts that fully exploit the potential of photogenerated electrons and holes in synergetic photocatalytic systems.

2. Results and discussion

2.1. Microstructures characterization

The Ni-CdS@$Ni(OH)_2$ heterojunction was synthesized through a solvothermal *in-situ* assembly approach, where porous ultrathin $Ni(OH)_2$ nanosheets were grown on the surface of Ni-CdS nanorods (see detailed in the supporting information). First, pristine CdS and Ni-doped CdS nanorods were synthesized using a hydrothermal and solvothermal methods, with ethylenediamine serving as a capping agent to preserve the regular morphology of the nanorods and to promote anisotropic growth. Transmission electron microscopy (TEM) indicates that the prepared CdS and Ni-CdS consisted of regular elongated (1D) nanorods Fig.s 1(a, b) with an average diameter of approximately 40 nm and lengths of several micrometers Figs. S1(a and b). The elongated 1D nanorods offer key advantages such as increased surface area, such as increased surface area, enhanced light absorption, and more catalytic surface-active sites. Subsequently, ultrathin layers of $Ni(OH)_2$ were grown on the surface of Ni-CdS nanorods using an *in-situ* self-assembly approach, involving a reaction between $Ni(NO_3)_2{\cdot}6H_2O$ and hexamethylenetetramine. This process resulted in the formation of hierarchical Ni-CdS@$Ni(OH)_2$ heterostructure nanorods, with strong interfacial interaction between Ni-CdS and $Ni(OH)_2$, facilitated by co-shared Ni atoms (Fig. 1c). Moreover, the thickness of the ultrathin nanosheet was tuned by varying the reaction time as can be seen in (Fig. S2). Besides, the $Ni(OH)_2$ thin nanospheres were also synthesized independently of the Ni-CdS nanorods, as shown in (Fig. S3**)**. Elemental mapping confirmed the presence of Cd, S, Ni, and O in the Ni-CdS@$Ni(OH)_2$ composite, implying the successful incorporation of Ni atoms into the CdS lattice (Fig. 1d). Further insights into the heterojunction were gained through high-resolution transmission electron microscopy (HRTEM) analysis. The incorporation of Ni ion into the CdS lattice results in a reduction of lattice spacing due to the smaller atomic size of Ni compared to Cd, as illustrated in (Fig. 1e**)**. Compared with the HRTEM images of pristine CdS (Fig. S4a**)**, Ni-CdS (Fig. S4b**)**, and $Ni(OH)_2$ (Fig. S4c), the HRTEM image of the Ni-CdS@$Ni(OH)_2$ composite clearly reveals lattice fringes corresponding to the Ni-CdS nanorods and $Ni(OH)_2$ nanosheets. Specifically, the Ni-CdS nanorods exhibit a lattice spacing of 0.324 nm corresponding to the (100) plane, while the $Ni(OH)_2$ nanosheets display a lattice spacing of 0.284 nm for the (001) plane. These observations confirm the well-crystallized structure and the intimate formation of the Ni-

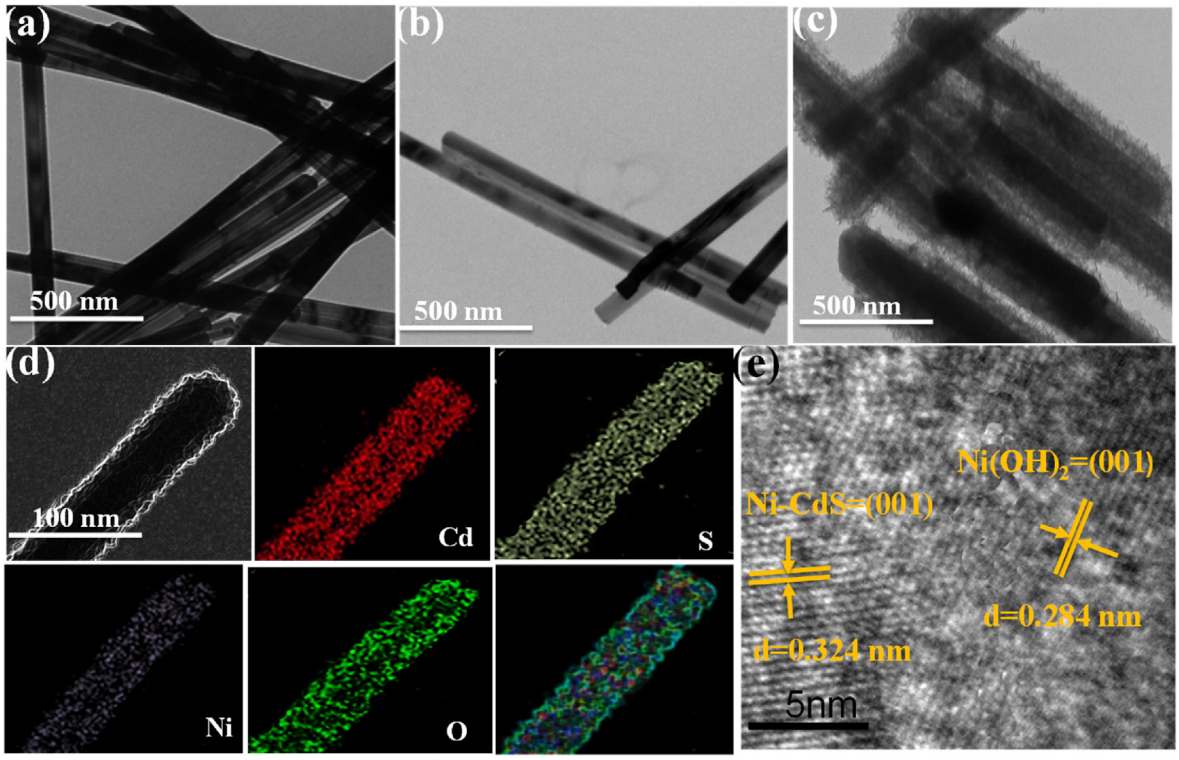

Fig. 1. (a–d) TEM images of (a) CdS, (b) Ni- CdS, (c,d) Ni- CdS@$Ni(OH)_2$ and elemental mapping; (e) HRTEM images of Ni-CdS nanorods and Ni-CdS@$Ni(OH)_2$ nanorods.

CdS@$Ni(OH)_2$ heterojunction.

To investigate the crystallinity and phase purity of the synthesized samples, X-ray diffraction patterns (XRD) was conducted (Fig. 2a). The XRD pattern of the pristine CdS perfectly matches the standard patterns of the hexagonal phase of CdS (PDF#77–2306), confirming its crystal structure. In contrast, the XRD pattern of Ni-CdS reveals the emergence of two distinct phases upon incorporating Ni ions into the CdS lattice. In which, the three main peaks corresponding to the (100), (002), and (101)

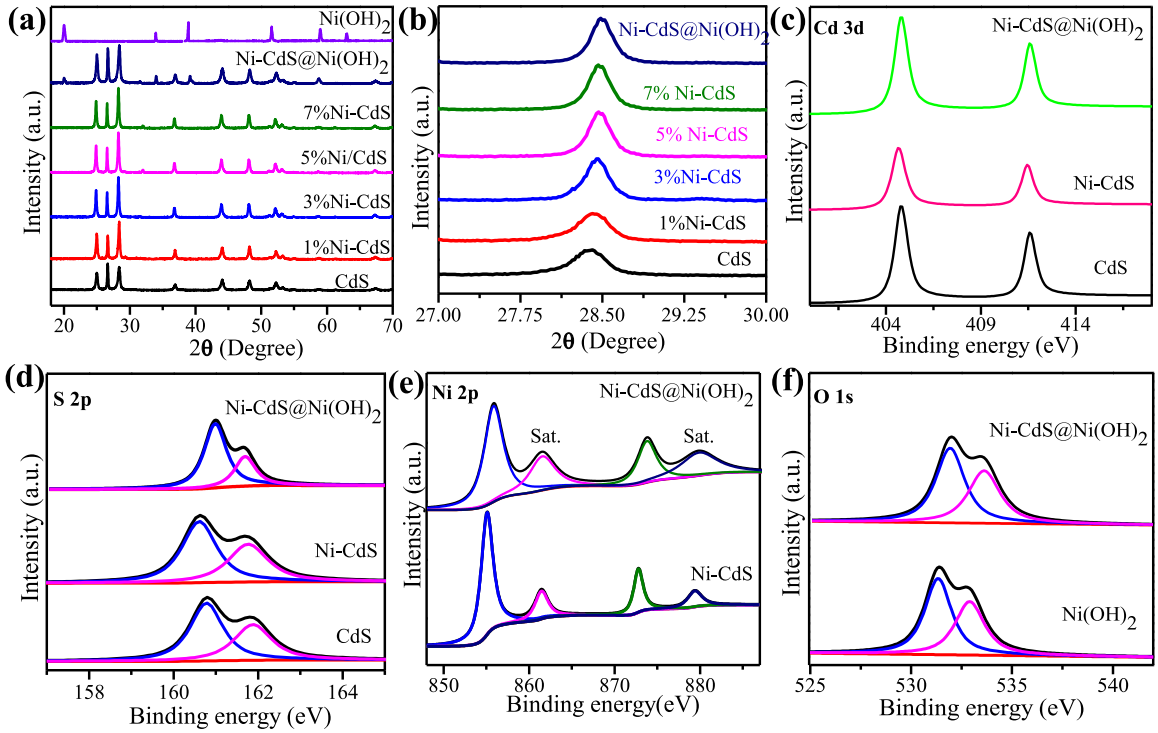

Fig. 2. (a) XRD patterns of the as-prepared materials; (b) Respective magnified XRD patterns in the range of 2θ=27–30 °; (c–f) XPS spectra of Cd 3 d (c), S 2p (d), Ni 2p (e), and O1s (f).

planes within the range of 20–35 °are associated with the hexagonal phase, while the peak at ≈32°, assigned to (200) plane, signifies the presence of cubic phase. Interestingly, the incorporation of Ni ions into the CdS lattice promote the phase transformation from hexagonal to a mixed hexagonal/cubic phase during hydrothermal synthesis process, resulting in different exposed facets. This mixed-phase structure favors the photogenerated charge separation during photocatalysis. Furthermore, the magnified XRD pattern of Ni-CdS (Fig. 2b**)** shows a shift in the main peaks [(100), (002), and (101)] within the 2θ range of 27–30 towards higher diffraction angles compared to pristine CdS (Fig. 2a**)**. This shift, attributed to the smaller ionic radius of Ni compared to Cd, suggests the successful incorporation of Ni atoms into the CdS crystal lattice. The XRD pattern of the $Ni(OH)_2$ nanosheet exhibits distinctive diffraction peaks as shown in (Fig. 2a**)**, which are indexed to the hexagonal phase of $Ni(OH)_2$ (JCPDS PDF#03–0177), confirming the crystalline structure of the material. Remarkably, the diffraction peaks of the Ni-CdS@$Ni(OH)_2$ heterojunction align well with the standard XRD patterns of the both Ni-CdS and $Ni(OH)_2$, indicating the successful formation of heterojunction without any impurities.

The surface chemical states and elemental composition of the samples CdS, Ni-CdS and Ni-CdS@$Ni(OH)_2$ were characterized by X-ray photoelectron spectroscopy (XPS). The XPS survey spectra (Fig. S5) provide a clear overview of the elemental composition. For CdS, only peaks corresponding to Cd and S were observed, confirming the purity of the material. As for Ni-CdS, an additional peak for Ni was detected, signifying the successful incorporation of Ni into the CdS lattice. The full XPS survey of the Ni-CdS@$Ni(OH)_2$ heterojunction displayed all characteristics peaks of Cd, S, Ni, and O, confirming the presence of both Ni-CdS and $Ni(OH)_2$ in the heterojunction. In the high resolution XPS analysis of CdS, binding energies of 411.61 eV and 404.86 eV were assigned to the Cd $3d_{3/2}$ and Cd $3d_{5/2}$ orbitals, respectively. Upon the introduction of Ni into the CdS crystal lattice (forming Ni-CdS), a shift to lower binding energies in the Cd 3 d peaks is observed (Fig. 2c**)**. This shift is attributed to increased electron cloud density surrounding the cadmium atoms due to electron donation by Ni, which disrupts the CdS electronic structure and enhances electron density within the material [31,34]. However, when the ultrathin nanosheet of $Ni(OH)_2$ is grown onto the surface of CdS nanorods, the binding energies of Cd $3d_{3/2}$ and Cd $3d_{5/2}$ shift to higher values once again, indicating a strong interaction and bonding between the Ni-CdS and $Ni(OH)_2$. Consistent with the Cd 3 d XPS results, the S 2p peaks in the Ni-CdS sample exhibit a negative shift in binding energy compared to pristine CdS (Fig. 2d). In the Ni-CdS@$Ni(OH)_2$ composite, the S 2p peaks shift towards higher binding energy, reflecting the stronger interfacial contact between the Ni-CdS nanorods and the $Ni(OH)_2$ nanosheet (Fig. 2e). Moreover, the XPS spectrum of O1s core level in the $Ni(OH)_2$ reveals characteristic peaks at 531.25 eV and 532.35 eV, which are consistent with previously reported values for nickel hydroxide [23,35,36]. As for the XPS spectra of O 1s in the Ni-CdS@$Ni(OH)_2$ heterojunction (Fig. 2f), a significant positive shift was observed. This shift indicates a strong interfacial interaction between the Ni-CdS core and the $Ni(OH)_2$ shell, highlighting the enhanced bonding and electron interaction at the interface.

2.2. Mechanism of charge carrier behavior

It is widely recognized that variations in binding energies (BEs) of elements within a heterostructure reflect changes in valence state or electron density, providing reliable indicators of electron transfer direction within the heterojunction [13,37–39]. Generally, the reduction of elements is associated with a decrease in binding energy (BE), whereas oxidation typically results in an increase in BE [40,41]. To probe the direction of charge transfer within the Ni-CdS@$Ni(OH)_2$ heterojunction, a comparative study of valence band XPS was performed. The results reveal enhanced electron density in the valence band XPS of Ni-CdS compared to pristine CdS. This enhancement in electron density in case of Ni doped CdS is attributed to the creation of hybrid state within the bandgap of CdS, leading to uneven distribution of charge carriers and the formation of internal built in-electric field. Besides, formation of interface states between Ni-CdS and $Ni(OH)_2$ likely influence the charge distribution at the interface and may affect the flat band potential [42,43]. The enhanced electron density observed in the valence band XPS of Ni-CdS compared to pristine CdS, which further increases after the growth of a thin nanosheet of $Ni(OH)_2$ (Fig. 3a**)**, is attributed to the formation of an external IEF at the heterojunction interface. These internal and external electric fields play a crucial role in accelerating photogenerated electron transfer, thereby promoting proton reduction, which aligns with the pervious report [16,44]. Besides, a p-type semiconductor, $Ni(OH)_2$, exhibits a Fermi level in the range of approximately 5.4–5.6 eV relative to the vacuum level [45,46], which is higher compared to the Fermi level of CdS (−4.5 eV vs vacuum) [46]. The disparity in Fermi levels between $Ni(OH)_2$ and CdS leads to the formation of a IEF at the Ni-CdS@$Ni(OH)_2$ interface. This electric field facilitates enhanced spatial separation of charge carriers, thereby promoting improved charge separation efficiency.

To investigate the light-harvesting properties of the materials, UV–vis absorption spectroscopy was employed in Fig. S6a. The pristine CdS exhibited an absorption edge at ≈530 nm, while Ni-CdS exhibits a slight red shift, which becomes more pronounced after the deposition of the $Ni(OH)_2$ ultrathin layer. As shown in Fig. S6b, the bandgaps of pristine CdS, Ni-CdS, and Ni-CdS@$Ni(OH)_2$ were determined to be approximately 2.4 eV, 2.36 eV, and 2.34 eV, respectively, using the Kubelka-Munk function. The observed bandgap narrowing enhances light absorption, promoting the generation of more photoexcited electrons. These results are consistent with the valence band XPS analysis. The conduction band positions of CdS and Ni-CdS were determined using Mott-Schottky plot analysis (Fig. S7a). As shown in Fig. S7b, the MS curve of $Ni(OH)_2$ shows a positive curve, indicating the conductive nature of the p-type semiconductor, which has a plate band potential of 1.15 eV vs. NHE. Pristine CdS shows a flat band potential (V_{fb}) around −0.6 eV, confirming its n-type semiconductor behavior. However, in Ni-CdS, the (V_{fb}) potential shifts to −0.92 eV, indicating enhanced n-type behavior. The flat band potential of Ni-CdS@$Ni(OH)_2$ is significantly altered due to the strong p-n heterojunction formed between Ni-CdS and $Ni(OH)_2$. The interface states between Ni-CdS and $Ni(OH)_2$ can affect charge distribution at the interface and potentially influence the flat band potential [47].

The electron transfer mechanism in the Ni-CdS@$Ni(OH)_2$ heterojunction was investigated to further validate the proposed charge transfer process using electron paramagnetic resonance (EPR) spectroscopy [48–50]. In this analysis, 5,5-dimethyl-1-pyrroline N-oxide (DMPO) was employed as a spin-trapping agent to detect the presence of superoxide radicals ($\bullet O_2^-$) and hydroxyl radicals (•OH), offering insights into charge carrier dynamics and the generation of reactive oxygen species (ROS) within the photocatalytic system.

Fig. 3b illustrates four distinct peaks corresponding to DMPO-$\bullet O_2^-$ signals for CdS, Ni-CdS, and Ni-CdS@$Ni(OH)_2$ under light irradiation. In contrast, DMPO-$\bullet O_2^-$ signals were observed for the pristine $Ni(OH)_2$ nanosheets, which can be attributed to the electrons in the conduction band can generate $\bullet O_2^-$. Besides, Fig. 3c illustrates that CdS, Ni-CdS, and Ni-CdS@$Ni(OH)_2$ exhibit signal peaks corresponding to DMPO-•OH, indicating the presence of hydroxyl radicals. In contrast, $Ni(OH)_2$ alone does not show any DMPO-•OH signal peaks. This absence can be attributed to its high reduction nature and limited oxidation potential, which restrict its ability to generate hydroxyl radicals.

Notably, the peak intensities for the Ni-CdS@$Ni(OH)_2$ hierarchical heterostructure were higher than those of CdS and Ni-CdS, indicating that dual electric fields suppress the recombination of photogenerated carriers by promoting unequal charge distribution. This suggests higher electron density on the Ni-CdS interface and a corresponding accumulation of photogenerated holes on the $Ni(OH)_2$ surface. These observations align with valence band XPS results. As illustrated in Fig. 3d, the EPR signal intensity of CdS is significantly lower than that of Ni-CdS, which is attributed to the built-in electric field generated by Ni

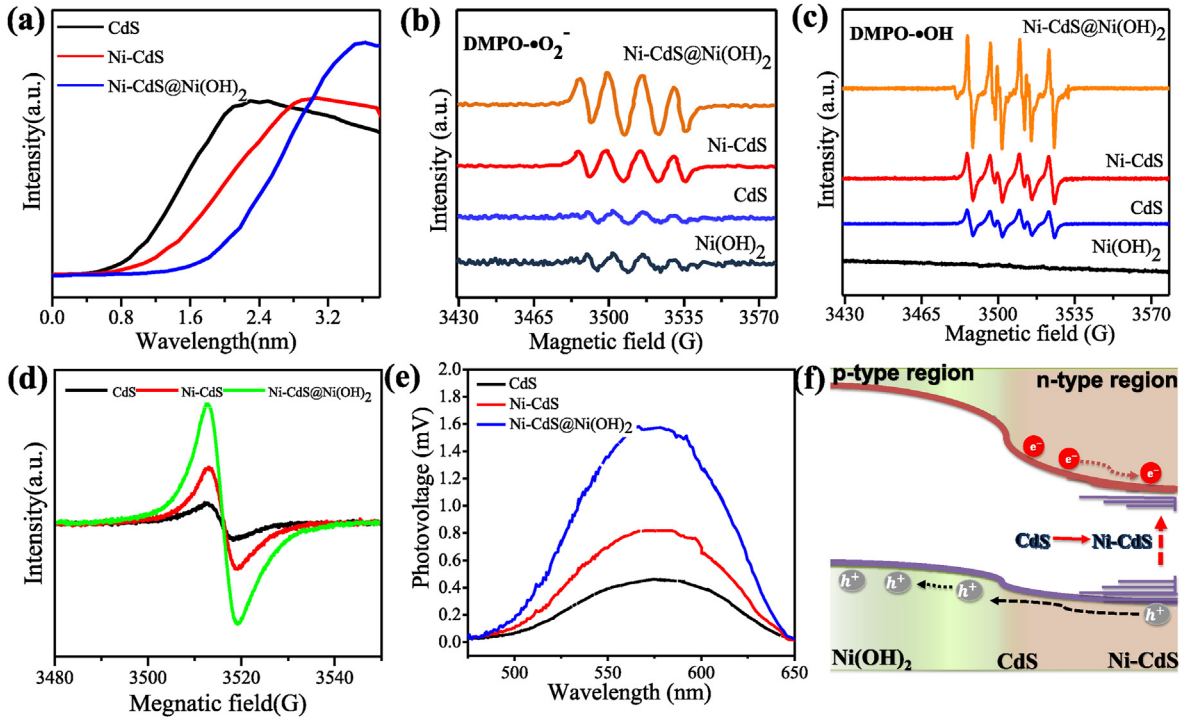

Fig. 3. (a) Valance band XPS of CdS, Ni-CdS, and Ni-CdS@Ni(OH)$_2$; (b) DMPO-•O_2^- in a saturated O_2 acetonitrile solution in the presence of CdS, Ni-CdS, Ni(OH)$_2$, and Ni-CdS@Ni(OH)$_2$; (c) DMPO-•OH detection in an acetonitrile/water dispersion (200:1 vol ratio) in the presence of CdS, Ni-CdS, Ni(OH)$_2$, and Ni-CdS@Ni(OH)$_2$; (d) EPR spectra of the CdS, Ni-CdS, and Ni-CdS@Ni(OH)$_2$ samples; (e) Surface photovoltage of the prepared samples, i.e., CdS, Ni-CdS, and Ni-CdS@Ni(OH)$_2$; (f) Schematic representation of the directional flow of photogenerated charges in Ni-CdS@Ni(OH)$_2$.

incorporation into the CdS lattice. This signal intensity is further enhanced following the introduction of the Ni(OH)$_2$ ultrathin nanosheet, indicating the presence of an interfacial built-in electric field. In the coupled CO_2 photoreduction and selective toluene oxidation system, singlet oxygen ($^1O_2$) selectively oxidizes toluene to benzaldehyde, while photogenerated holes (h^+) facilitate toluene activation and proton generation for CO_2 reduction. This synergistic mechanism enhances both reaction pathways, ensuring high selectivity and efficiency in the dual-functional photocatalytic process.

To further elucidate the efficiency of photogenerated charge transport in CdS, Ni-CdS, and Ni-CdS@Ni(OH)$_2$, surface photovoltage (SPV) spectra were analyzed (Fig. 3e). Ni-CdS exhibited a significantly higher SPV response than pristine CdS, implying a substantial enhancement in photogenerated charge carrier density. The growth of a porous Ni(OH)$_2$ nanosheet resulted in a further enhancement of the SPV response, confirming a higher concentration of photogenerated electrons on the surface of Ni-CdS@Ni(OH)$_2$. Thus, Ni incorporation induced internal built in-electric field and the ultrathin Ni(OH)$_2$ nanosheet induce interfacial IEF, synergistically induced dual built-in electric fields that play a key role in photo-induced electron transfer. Similarly, the zeta potentials of CdS, Ni-CdS, and Ni-CdS@Ni(OH)$_2$ were measured as −2.4 mV, −4.5 mV, and −8.7 mV, respectively (Fig. S8). Under visible light illumination ($\lambda \geq 420$ nm), the Ni-CdS crystal lattice generates photoexcited electron-hole pairs. Given its wide bandgap (~3.4 eV), determined by Kubelka-Munk analysis in Figs. S9(a and b), Ni(OH)$_2$ remains inactive in this wavelength range. However, the interfacial contact between Ni-CdS and Ni(OH)$_2$ creates a IEF due to favorable energy level alignment (with Ni-CdS having more positive valence and conduction band edges), promotes efficient charge separation and transfer. This directional flow of photogenerated charges is illustrated in Fig. 3f. The specific surface areas of CdS, Ni-CdS, and Ni-CdS@Ni(OH)$_2$ were determined via nitrogen adsorption-desorption isotherm analysis (Fig. S10). The isotherms exhibited a Type II shape, indicative of macroporosity, and Type H3 hysteresis loops, suggesting mesopores. BET analysis revealed surface areas of 38.56 m^2/g, 39.55 m^2/g, and 222.34 m^2/g for CdS, Ni-CdS, and Ni-CdS@Ni(OH)$_2$, respectively. The significantly larger surface area of Ni-CdS@Ni(OH)$_2$ provides more active sites, enhancing CO_2 adsorption and subsequent photocatalytic reduction. As shown in Fig. S11, the Ni-CdS@Ni(OH)$_2$ composite demonstrated significantly enhanced CO_2 adsorption compared to bare CdS and Ni-CdS. This improvement is attributed to the synergistic effect of the enlarged specific surface area and favorable modification of the local chemical environment by the alkaline ultrathin Ni(OH)$_2$ nanosheets, which facilitate the adsorption of acidic CO_2 molecules.

2.3. Evaluation of bifunctional photocatalytic performance

The potential of the Ni-CdS@Ni(OH)$_2$ heterostructure with dual IEFs was evaluated for an integrated photoredox reaction of CO_2 photoreduction coupled with oxidation of toluene under visible light irradiation in a sacrificial reagents free system. The photocatalytic results in Fig. 4a indicate that the pristine CdS displayed negligible activity for both CO_2 reduction and toluene oxidation, while Ni(OH)$_2$ only produced trace amounts of BD from toluene oxidation and lacked the required reduction potential to reduce CO_2. However, the incorporation of Ni into the CdS crystal lattice with optimum Ni doping concentration of 5%, as determined using inductively coupled plasma-atomic emission spectrometry (ICP-AES) showed enhancement in both CO_2 reduction and toluene oxidation to some extent due to the formation of an internal built-in electric field that facilitated charge separation, thus boosting photocatalytic performances as shown in (Fig. S12). Furthermore, the rational growth of ultrathin Ni(OH)$_2$ nanosheets on the surface of Ni-CdS nanorods generates an additional interfacial electric field. The interplay between this interfacial electric field and the intrinsic electric field within the Ni-CdS nanorods creates synergistic driving forces for the efficient separation and transport of photogenerated electron-hole pairs. Consequently, the Ni-CdS@Ni(OH)$_2$ heterostructure exhibited remarkable performance, achieving simultaneous CO_2 reduction (427 μmol g^{-1} h^{-1})

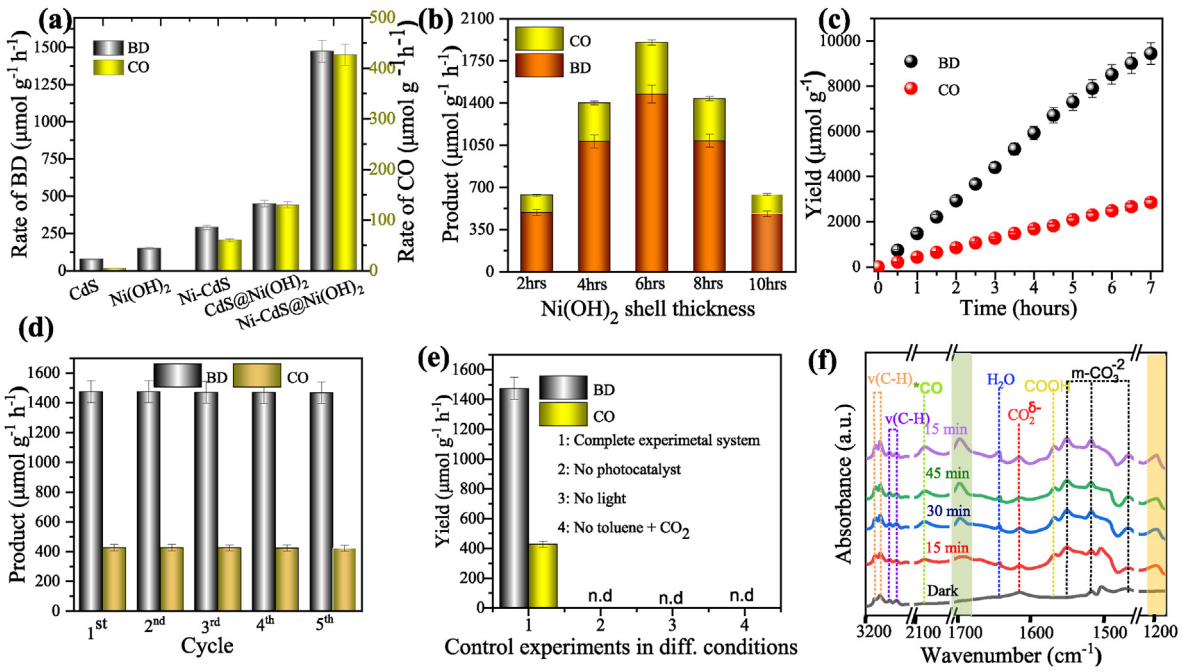

Fig. 4. (a) Visible-light driven redox reaction performed at CdS, Ni-CdS, and Ni-CdS@$Ni(OH)_2$; (b) Photoredox reaction performances with different $Ni(OH)_2$ growth times for optimization of $Ni(OH)_2$ nanosheet; (c) Yield of the product obtained as a function of reaction time; (d) Recyclability of the optimized photocatalyst; (e) Photoredox performance at various reaction conditions; (f) *In-situ* diffuse reflectance infrared fourier transform spectra acquired under visible light irradiation of the Ni-CdS@$Ni(OH)_2$ p-n heterojunction in a toluene and CO_2 mixture.

and selective toluene oxidation to BD (1 476 μmol g^{-1} h^{-1} with 85% selectivity). Benzyl alcohol was also produced as a byproduct at a rate of 395 μmol g^{-1} h^{-1}, which outperforms the majority of state-of-the-art CdS based photocatalysts, as detailed in Tables S1 and S2 of the Supporting Information. To assess the impact of $Ni(OH)_2$ nanosheet thickness on the photocatalytic performance of Ni-CdS nanorods, various growth times (ranging from 2 to 10 h) were studied. A 6-h growth time was found to produce the optimal nanosheet thickness, maximizing efficiency of both CO_2 photoreduction and selective toluene oxidation. This is attributed to the formation of an ultrathin, porous $Ni(OH)_2$ nanosheet, which established a strong and uniform interface, significantly improving charge separation (Fig. 4b). The percentage of $Ni(OH)_2$ nanosheets was quantified using Inductively coupled plasma optical emission spectroscopy (ICP-OES), revealing a composition of 6wt% in the optimal nanosheet thickness. The long-term stability of the Ni-CdS@$Ni(OH)_2$ heterostructure was evaluated by extended photocatalytic experiments (Fig. 4c and d), which showed sustained production of CO and BD without any significant decline, indicating excellent photostability of the heterojunction. Additionally, TEM and XRD analyses performed after the photocatalytic reactions (Fig. S13) revealed that the structure and composition of the Ni-CdS@$Ni(OH)_2$ heterostructure remained intact, even after repeated use. In addition to XRD and TEM, the XPS analysis presented in Fig. S14 showed the chemical states of Cd, S, and Ni in the Ni-CdS@$Ni(OH)_2$ before and after the photocatalytic reaction. The spectra confirm that the elemental composition remains largely unchanged, indicating the stability of the synthesized materials. While slight shifts in binding energies and peak intensities are observed after the reaction, which are due to minor surface modifications rather than significant degradation. These results further validate the structural integrity and durability of the materials, demonstrating their sustained effectiveness in photocatalytic applications even after prolonged operational cycles.

Control experiments (Fig. 4e) confirmed that no photocatalytic activity occurred without light or the photocatalyst, while the full experimental setup yielded CO, BD, and benzyl alcohol. Isotope-labeling experiments (Fig. S15) verified that the CO originated from CO_2 reduction. Based on these results, a proposed mechanism for the CO_2 photoreduction integrated with selective toluene oxidation using the Ni-CdS@$Ni(OH)_2$ hierarchical nanoarchitecture is graphically illustrated in Fig. S16**.** Moreover, to get deeper insights into the dynamic changes occurring during the reaction process, time-resolved *in-situ* diffuse reflectance infrared Fourier-transform spectroscopy (DRIFTS) was employed to investigate the reaction mechanism and identify the adsorbed intermediates involved in the photocatalytic redox reactions [51–53]. As shown in Fig. 4f, when the Ni-CdS@$Ni(OH)_2$ heterojunction was exposed to a CO_2 and toluene mixture, characteristic absorption peaks were observed at 1613 cm^{-1} attributed to the formation of $CO_2^{\delta-}$ species [54]. Peaks at 3076 and 3038 cm^{-1} corresponded to the C–H stretching vibrations of the aromatic ring, while peaks at 2943 and 2882 cm^{-1} were associated with the methyl group in toluene [55]. Upon light irradiation, new absorption peaks emerged, signaling the formation of reaction intermediates. A peak at 1557 cm^{-1} was assigned to *COOH species, while peaks at 1 543, 1 513, and 1458 cm^{-1} were attributed to monodentate carbonate (m-CO_3^{2-}) groups. Additionally, a peak at 2078 cm^{-1} indicated the presence of *CO species. These spectroscopic observations provide compelling evidence for the formation and involvement of these intermediates in the photocatalytic reaction process [56,57]. Furthermore, additional absorption peaks at 1697 cm^{-1} and 1212 cm^{-1} were observed, attributed to the carbonyl (C=O) stretching vibration in BD and the C-O stretching vibration in BA, respectively.

2.4. Photogenerated charge separation

To elucidate the relationship between the synergy of the dual electric fields and the effect on charge transfer in Ni-CdS@$Ni(OH)_2$ heterojunction, density functional theory (DFT) calculations were conducted. Initially, the impact of the incorporation of Ni-doping on the spin-polarized electric field of Ni-CdS was calculated. As shown in Fig. S17(a, b), pristine CdS exhibited the symmetric spin-up projected density of states (PDOSs), while in Ni-CdS the spin-up states dominate near the Fermi level, suggesting the presence of spin-polarized electrons. This spin polarization arises due to Ni doping. The dominance of Ni d-

orbital contributions in the PDOS near the Fermi level is evident in the graph, where the Ni d-orbital states overlap with the conduction band. This overlap signifies that Ni doping introduces localized electronic states that influence the electronic properties of the material. The spin polarization induced by Ni doping leads to an imbalance in the charge density of electrons. This charge imbalance generates a spin-polarized electric field, thus endorsing the photogenerated electrons to move to the conduction band in the interior of Ni-incorporated CdS. As shown in Fig. S18, after the growth of ultrathin nanosheets of p-type $Ni(OH)_2$ on the surface of Ni-CdS, a reduction in bandgap is observed which creates an interfacial IEF leading to boosted electrical conductivity and photogenerated charge separation. As depicted in Fig. S19 $Ni(OH)_2$, a wide-bandgap p-type semiconductor, plays a pivotal role in the formation of an interfacial IEF within the Ni-CdS@$Ni(OH)_2$ heterojunction. This internal electric field serves as a driving force, facilitating the efficient spatial separation and subsequent propagation of photogenerated charge carriers, thereby enhancing the overall charge transport dynamics within the composite system. Meanwhile, the Ni incorporation played a pivotal role in generating the spin-polarized electric field, while the ultra-thin nanosheet of $Ni(OH)_2$ contributed to the formation of an interfacial electric field. The simulated work functions (Φ) for pristine CdS, Ni-doped CdS, and $Ni(OH)_2$ were determined to be 5.62 eV, 5.26 eV, and 4.61 eV, respectively, as shown in Figs. S20(a–c). It can be concluded that Ni doping not only elevated the Fermi level of Ni-CdS to promote the acceleration from the valence band to the conduction band [58], but also maintained the greater difference between Ni-doped CdS and $Ni(OH)_2$. It is a general phenomenon that the interaction between two semiconductors with differing Fermi energy levels is widely recognized to generate a EF at their interface. Moreover, a greater difference in Fermi levels results in a stronger EF. Besides, Fig. S21 illustrates the charge density difference ($\Delta\rho$) along the Z-axis direction in the Ni-CdS @$Ni(OH)_2$ heterojunction system, which provides critical insight into charge redistribution at the interface. This figure demonstrates the redistribution of charge across the Ni-CdS@$Ni(OH)_2$ heterojunction. The distinct patterns of electron accumulation and depletion highlight the presence of a built-in electric field, driven by the interfacial interactions and the spin-polarized electric field induced by the Ni dopant. These features play a critical role in facilitating efficient charge separation and transport.

To better understand the enhanced simultaneous photocatalytic redox reactions in the Ni-CdS@$Ni(OH)_2$ heterojunction, the charge carrier kinetics was investigated using photoelectrochemical techniques. The results shown in Fig. 5 (a, b) reveals that the dominant emission peak for pristine CdS, located at 532 nm, corresponds to the radiative recombination of photogenerated electron-hole pairs through band-to-band transitions. The intensity of this peak reflects the high recombination rate of pristine CdS. Upon Ni incorporation into the CdS lattice, a significant reduction in PL intensity was observed, indicating partial suppression of recombination. Furthermore, growth of the $Ni(OH)_2$ nanosheet on the Ni-CdS significantly reduces the PL intensity, suggesting enhanced charge separation efficiency at the material interfaces due to the introduction of Ni and subsequent encapsulation. Time-resolved photoluminescence (TRPL) spectroscopy was employed to further investigate the charge carrier dynamics and separation efficiency in Ni-CdS@$Ni(OH)_2$, Ni-CdS, and pristine CdS. The decay kinetics (Fig. 5c and Table S3) revealed a notably longer average carrier lifetime (τ) for Ni-CdS@$Ni(OH)_2$ (8.60 ns) compared to Ni-CdS (6.30 ns) and pristine CdS (5.21 ns), reflecting the improved separation of photogenerated electron-hole pairs. This enhancement is attributed to the stronger interfacial contact and the shared Ni component between the core and shell materials. Electrochemical impedance spectroscopy (EIS) results (Fig. 5d) further confirmed this enhancement, as Ni-CdS@$Ni(OH)_2$ exhibited a significantly smaller high-frequency semicircle, indicating lower charge-transfer resistance compared to Ni-CdS and pristine CdS. This reflects a faster rate of photogenerated charge transfer at the interface within the Ni-CdS@$Ni(OH)_2$ photoanode. Transient photocurrent (TPC) spectroscopy (Fig. 5e) also supported these findings, as the photocurrent density of Ni-CdS@$Ni(OH)_2$ was substantially higher than that of Ni-CdS and pristine CdS. This increase highlights more efficient charge separation and transfer in the Ni-CdS@$Ni(OH)_2$ photoanode, further aided by the interfacial charge transfer between CdS and $Ni(OH)_2$, with the shared Ni atom at the interface playing a key role. To further explore the impact of

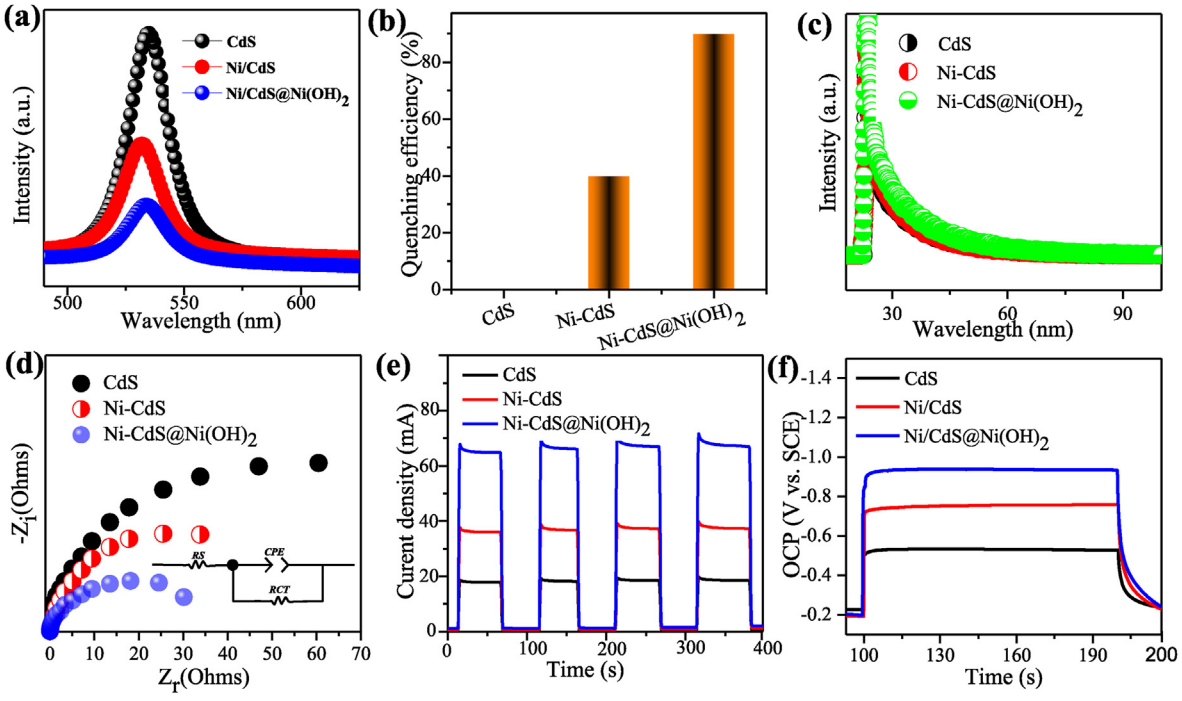

Fig. 5. Techniques used for measuring charge separation in the prepared materials. (a) PL emission spectra; (b) Quenching efficiency of the as synthesized materials; (c) Time-resolved photoluminescence, (d) electrochemical impedance spectroscopy Nyquist plots of the prepared materials; (e) Photocurrent responses under chopped visible light irradiation; (f) Open circuit potential measurements for the as synthesized materials.

Ni incorporation and $Ni(OH)_2$ nanosheet deposition on charge separation, open-circuit potential (OCP) measurements were conducted (Fig. 5f). This technique assesses the difference in Fermi levels between the working electrode and the counter electrode under illumination. The progressive accumulation of electrons in the photoanode, as driven by redox equilibration, increases the OCP. A more positive OCP reflects enhanced electron accumulation and charge separation efficiency, with slower recombination and a more efficient rise in photovoltage over time. These observations align well with the PL, TRPL, EIS, and TPC results, collectively indicating that the introduction of the $Ni(OH)_2$ nanosheet facilitates charge separation and minimizes recombination losses, driving the overall improvement in photocatalytic performance [59,60]. Fig. S22a presents the linear sweep voltammetry (LSV) curves, illustrating the current density ($mA{\cdot}cm^{-2}$) as a function of potential (V vs. RHE) for different photocatalyst materials. Among them, pristine CdS exhibits the highest onset potential and the lowest current density, indicating limited charge separation efficiency and catalytic activity. The incorporation of Ni into CdS (Ni-CdS) enhances the current density, suggesting an improvement in charge transport and interfacial charge transfer processes. Notably, the Ni-CdS@$Ni(OH)_2$ composite demonstrates the highest current density, implying a substantial enhancement in electrochemical activity. Besides, the Tafel slopes, derived from linear sweep voltammetry (LSV) curves as depicted in Fig. S22b, provide insight into the electrocatalytic behavior. The Tafel slope for Ni-CdS@$Ni(OH)_2$ (522 mV dec^{-1}) is smaller compared to those of CdS (635 mV dec^{-1}) and Ni-CdS (575 mV dec^{-1}). The reduced overpotential and smaller Tafel slope observed for Ni-CdS@$Ni(OH)_2$ suggest an enhancement in the charge carrier migration and separation. This improvement is attributed to the dual electric fields generated by the incorporation of Ni into the CdS lattice and the growth of a thin nanosheet on the surface of the Ni-CdS nanorods, which collectively facilitate the electrochemical process.

This remarkable improvement can be attributed to the formation of dual built in-electric fields at the heterointerfaces, which facilitate charge separation and suppress charge recombination. The Ni modification induces an internal electric field at the Ni-CdS interface, promoting directional charge migration, while the deposition of $Ni(OH)_2$ generates an additional electric field, further accelerating the extraction and transport of photogenerated carriers. Consequently, the synergistic effect of these dual electric fields lowers the overpotential and enhances electron transport kinetics, thereby significantly improving the overall photocatalytic performance. Furthermore, the presence of $Ni(OH)_2$ in the form thin hierarchical porous nanosheet provides active sites that facilitate electron transfer and surface reaction kinetics, contributing to the superior electrochemical response observed in the Ni-CdS@$Ni(OH)_2$ system.

2.5. Bifunction reaction mechanism

Based on the obtained results, a proposed mechanism for bifunctional photocatalytic CO_2 reduction coupled with selective toluene oxidation by the Ni-CdS@$Ni(OH)_2$ system is schematically portrayed in Fig. 6. Under visible light irradiation, Ni-CdS generates photoexcited electron-hole pairs. These charge carriers are effectively transferred to the Ni sites, facilitated by a polarized built-in electric field induced by the incorporation of Ni ions into the CdS lattice. This polarized electric field imbalances the photogenerated electron-hole pairs, driving the electrons towards the conduction band of Ni-CdS. Furthermore, $Ni(OH)_2$ is a p-type semiconductor with a plate band potential of 1.15 eV vs. NHE, as revealed by the MS plot in Fig. S7b. The bandgap energy derived from the UV–vis absorption spectrum is (3.4 eV), as illustrated in Fig. S9, where conduction band minimum (CBM) and valence band maximum (VBM) of $Ni(OH)_2$ nanosheets were determined to be −2.58 V and 0.82 V versus the Normal Hydrogen Electrode (NHE), respectively. While Ni-CdS is an n-type semiconductor whose conduction band minimum (CBM) and valence band maximum (VBM) of Ni-CdS (−1.47 V vs NHE and 0.92 eV vs NHE, respectively. Therefore, the band alignment within the Ni-CdS@$Ni(OH)_2$ heterojunction is a type-II configuration, as evidenced by

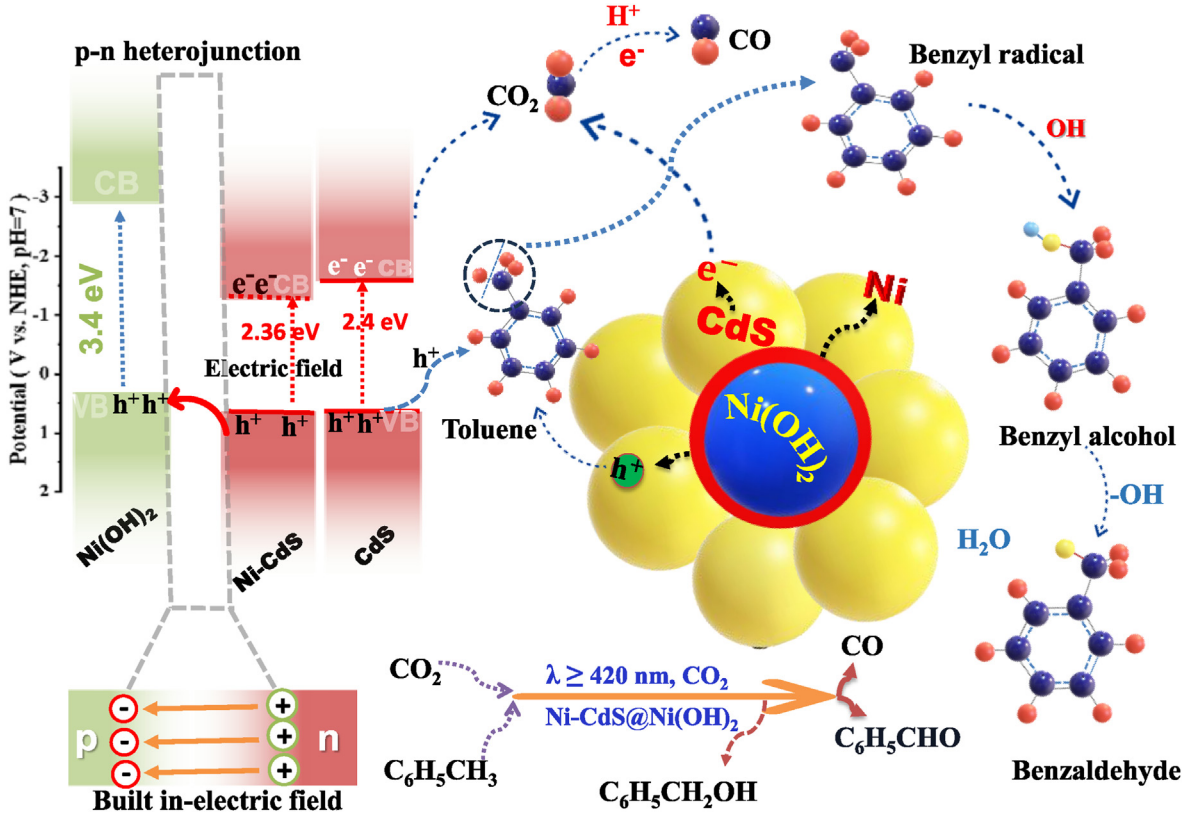

Fig. 6. Proposed photoredox mechanism on Ni-CdS@$Ni(OH)_2$ in visible-light driven CO_2 photoreduction integrated with toluene oxidation.

the band structures of $Ni(OH)_2$ and Ni-CdS. Despite its wide bandgap of 3.4 eV, the $Ni(OH)_2$ ultrathin nanosheet can still play a crucial role in photocatalytic processes within the Ni-CdS@$Ni(OH)_2$ heterojunction due to the favorable band alignment and strong interfacial contact between the p-type $Ni(OH)_2$ and n-type Ni-CdS, which together form a p-n junction. This results in the valence band (VB) and conduction band (CB) edges of Ni-CdS being more positive than those of $Ni(OH)_2$. Consequently, holes generated in the valence band of Ni-CdS are efficiently transferred to $Ni(OH)_2$, facilitating charge separation. This charge transfer renders Ni-CdS more negatively charged and $Ni(OH)_2$ more positively charged, inducing an interfacial built-in electric field within the heterojunction. The synergistic effect of this interfacial electric field, combined with the intrinsic built-in electric field from nickel doping, accelerates electron migration to the Ni sites, where proton reduction occurs. The highly oxidative photoinduced holes then react with the C-H bond in toluene, forming phenyl methylene radicals (•CH_2Ph) and protons. Simultaneously, the photogenerated electrons reduce CO_2 molecules and protons from toluene to form CO and water, respectively. The photoinduced holes also react with water, generating hydroxyl radicals (•OH), which are key reactive species for oxidizing the benzyl group into benzyl radicals. These highly reactive benzyl radicals further react with hydroxyl radicals to form benzyl alcohol (BA), which subsequently undergoes oxidation to produce the more stable BD. This dual reaction mechanism highlights the efficient charge separation and catalytic activity of the Ni-CdS@$Ni(OH)_2$ heterojunction.

3. Conclusion

In summary, a novel nanostructure of Ni-CdS@$Ni(OH)_2$ was rationally synthesized via a solvothermal process followed by *in-situ* assembly, designed to enhance visible-light-driven CO_2 photoreduction coupled with selective toluene oxidation. This system utilizes dual IEFs, acting as dual driving forces for efficient spatial charge separation and transfer, as confirmed by various experimental characterizations and theoretical simulations. These dual IEFs not only induce spatial charge separation but also enhance the redox potential of the Ni-CdS@$Ni(OH)_2$ heterojunction, enabling simultaneous oxidation and reduction reactions using CO_2 and toluene as reactants eliminating the needs of sacrificial reagent. As a proof of concept, the Ni-CdS@$Ni(OH)_2$ photocatalyst exhibits outstanding performance, achieving CO production at a rate of 427 μmol g^{-1} h^{-1} and a BD yield of 1474 μmol g^{-1} h^{-1} with 85% selectivity. This study provides valuable insights into the design of efficient multifunctional photocatalysts, showcasing the potential of synergistic systems and optimized photogenerated carriers for advancing the field of photocatalytic applications.

4. Experimental section

4.1. Synthesis of CdS nanorods

In a standard experimental procedure CdS nanorods were synthesized by following a reported methodology with modification [61]. Typically, 0.25 g of cadmium acetate dihydrate and 0.15 g of thiourea were combined in a beaker containing 30 mL of ethylenediamine and stirred for 30 min at room temperature. The mixture was then transferred to a 100 mL Teflon-lined stainless-steel autoclave that was pre-filled with ethylenediamine to 60% of its volume. The autoclave was heated at 180 °C for 24 h. After cooling to room temperature, the yellow product was washed three times each with deionized water and absolute ethanol to remove any remaining organic residues. Finally, the product was dried at 60 °C in a vacuum oven for 8 h.

4.2. Synthesis of Ni-doped CdS nanorods

Ni-doped CdS photocatalysts were prepared via a one-step solvothermal method following a reported method with minor modification [62], Cadmium acetate dihydrate $(CH_3COO)_2Cd{\cdot}2H_2O$ (6 mmol) and nickel nitrate hexahydrate $Ni(NO_3)_2{\cdot}6H_2O$ (Ni/Cd + Ni molar ratios of 1, 3, 5, 7, and 9%) were combined with thiourea (18 mmol) in 40 mL of ethylenediamine and stirred to form a homogeneous solution. This solution was then transferred to a 100 mL Teflon-lined autoclave and heated at 180 °C for 24 h. After cooling, the products were isolated by centrifugation, washed with ethanol, and deionized water, and dried at 60 °C under vacuum. Pristine CdS was synthesized in the absence of the Ni precursor.

4.3. Synthesis of Ni-CdS@$Ni(OH)_2$

The composite photocatalyst was synthesized by following a methodology used previously with slight modification [63]. Typically, 500 mg of the pre-synthesized Ni-CdS nanorods were dispersed in 200 mL of deionized water with stirring, followed by the addition of 3.75 mmol of Ni $(NO_3)_2{\cdot}6H_2O$ and stirred for 30 min. Afterword, 100 mL of an aqueous solution containing 0.375 mmol of $C_6H_5O_7Na_3$ and 3.75 mmol of hexamethylenetetramine was dropped into the mixture and stirred for an additional hour. The resulting solution was then heated to 90 °C and maintained under vigorous stirring for different time duration. After cooling to 25 °C, the sample was collected by centrifugation, washed multiple times with deionized water, and dried in a vacuum at 60 °C.

4.4. $Ni(OH)_2$ nanosheets synthesis

The synthesis procedure of $Ni(OH)_2$ ultrathin nanosheets was the same as that of Ni-CdS@$Ni(OH)_2$, except that Ni-CdS was not added.

CRediT authorship contribution statement

Khakemin Khan: Writing – review & editing, Writing – original draft, Methodology, Conceptualization. **Ahmed Mahmood Idris:** Writing – review & editing, Methodology, Formal analysis, Data curation. **Haseebul Hassan:** Writing – review & editing, Formal analysis, Data curation. **Sajjad Haider:** Conceptualization, Validation, Writing – review & editing, Methodology, Funding acquisition. **Salah Ud-Din Khan:** Conceptualization, Data curation, Review & editing, Investigation. **Antonio Miotello:** Writing – review & editing, Validation, Supervision, Project administration, Funding acquisition, Conceptualization. **Ihsanullah Khan:** Software, Formal analysis, Data curation.

Acknowledgements

The authors sincerely appreciate funding from "Producing Hydrogen in Trentino-H2@TN" (PAT-Trento) through the research grant (SAP 40104237) and Researchers Supporting Project number (RSP2025R399), King Saud University, Riyadh, Saudi Arabia.

Appendix A. Supplementary data

Supplementary data to this article can be found online at https://doi.org/10.1016/j.apmate.2025.100284.

References

[1] C. Tian, R. Dorakhan, J. Wicks, Z. Chen, K.S. Choi, N. Singh, J.A. Schaidle, A. Holewinski, A. Vojvodic, D.G. Vlachos, Progress, and roadmap for electro-privileged transformations of bio-derived molecules, Nat. Catal. 7 (2024) 350–360.
[2] F. Raziq, K. Khan, S. Ali, S. Ali, H. Xu, I. Ali, A. Zada, P.M. Ismail, A. Ali, H. Khan, Accelerating CO_2 reduction on novel double perovskite oxide with sulfur, carbon incorporation: synergistic electronic and chemical engineering, J. Chem. Eng. 446 (2022) 137161.
[3] L. Chen, M.A. Maigbay, M. Li, X. Qiu, Synthesis and modification strategies of g-C_3N_4 nanosheets for photocatalytic applications, Adv.Powder Mater. 3 (2024) 100150.
[4] J.D. Xiao, R. Li, H.L. Jiang, Metal-organic framework-based photocatalysis for solar fuel production, Small Methods 7 (2023) 2201258.

[5] Y.Z. Cheng, W. Ji, P.Y. Hao, X.H. Qi, X. Wu, X.M. Dou, X.Y. Bian, D. Jiang, F.T. Li, X.F. Liu, A fully conjugated covalent organic framework with oxidative and reductive sites for photocatalytic carbon dioxide reduction with water, Angew. Chem. Int. Ed. 62 (2023) 202308523.

[6] Z. Wu, J. Shen, C. Li, C. Zhang, K. Feng, Z. Wang, X. Wang, D.M. Meira, M. Cai, D. Zhang, Mo_2TiC_2 MXene-supported Ru clusters for efficient photothermal reverse water-gas shift, ACS Nano 17 (2022) 1550–1559.

[7] L. Yuan, M.Y. Qi, Z.R. Tang, Y.J. Xu, Coupling strategy for CO_2 valorization integrated with organic synthesis by heterogeneous photocatalysis, Angew. Chem. Int. Ed. 133 (2021) 21320–21342.

[8] J.H. Docherty, T.M. Lister, G. Mcarthur, M.T. Findlay, P. Domingo-Legarda, J. Kenyon, S. Choudhary, I. Larrosa, Transition-metal-catalyzed C–H bond activation for the formation of C–C bonds in complex molecules, Chem. Rev. 123 (2023) 7692–7760.

[9] H. Liao, K. Huang, W. Hou, H. Guo, C. Lian, J. Zhang, Z. Liu, L. Wang, Atmosphere engineering of metal-free Te/C_3N_4 pn heterojunction for nearly 100% photocatalytic converting CO_2 to CO, Adv. Powder Mater. 3 (2024) 100243.

[10] E. Gong, S. Ali, C.B. Hiragond, H.S. Kim, N.S. Powar, D. Kim, H. Kim, S.I. In, Solar fuels: research and development strategies to accelerate photocatalytic CO_2 conversion into hydrocarbon fuels, J. Energy Environ. Sci. 15 (2022) 880–937.

[11] T. Huang, Z. Huang, X. Yang, S. Yang, Q. Gao, X. Cai, Y. Liu, Y. Fang, S. Zhang, S. Zhang, Green and regulable synthesis of CdNCN on CdS semiconductor, atomic-level heterostructures for enhanced photocatalytic hydrogen evolution, Adv. Powder Mater. 3 (2024) 100242.

[12] H. Huang, J. Zhao, Y. Du, C. Zhou, M. Zhang, Z. Wang, Y. Weng, J. Long, J. Hofkens, J.A. Steele, Direct Z-scheme heterojunction of semicoherent $FAPbBr_3/Bi_2WO_6$ interface for photoredox reaction with large driving force, ACS Nano 14 (2020) 16689–16697.

[13] H. Zhang, Y. Gao, S. Meng, Z. Wang, P. Wang, Z. Wang, C. Qiu, S. Chen, B. Weng, Y.M. Zheng, Metal sulfide S-scheme homojunction for photocatalytic selective phenylcarbinol oxidation, Adv. Sci. 11 (2024) 2400099.

[14] S. Xu, G. Jiang, H. Zhang, C. Gao, Z. Chen, Z. Liu, J. Wang, J. Du, B. Cai, Z. Li, Boosting photocatalytic CO_2 methanation through interface fusion over CdS quantum dot aerogels, Small 20 (2024) 2400769.

[15] S. Thakur, A. Ojha, S.K. Kansal, N.K. Gupta, H.C. Swart, J. Cho, A. Kuznetsov, S. Sun, J. Prakash, Advances in powder nano-photocatalysts as pollutant removal and as emerging contaminants in water: analysis of pros and cons on health and environment, Adv. Powder Mater. (2024) 100233.

[16] K. Khan, Z.U. Rehman, S. Yao, M. Nawaz, M. Orlandi, A. Miotello, M. Ullah, K. Ullah, A.A. Alanazi, M.E. Zaki, Boosting visible-light-driven photocatalytic H_2 production by optimizing surface hydrogen desorption of NiS/CdS-P photocatalyst, Int. J. Hydrogen Energy 80 (2024) 427–434.

[17] K. Khan, X. Tao, M. Shi, B. Zeng, Z. Feng, C. Li, R. Li, Visible-light-driven photocatalytic hydrogen production on $Cd_{0.5}Zn_{0.5}S$ nanorods with an apparent quantum efficiency exceeding 80%, Adv. Funct. Mater. 30 (2020) 2003731.

[18] X. Liu, Y. Zhao, X. Yang, Q. Liu, X. Yu, Y. Li, H. Tang, T. Zhang, Porous Ni_5P_4 as a promising cocatalyst for boosting the photocatalytic hydrogen evolution reaction performance, Appl. Catal., B 275 (2020) 119144.

[19] K. Li, H. Pan, F. Wang, Z. Zhang, S. Min, In-situ exsolved NiS nanoparticle-socketed CdS with strongly coupled interfaces as a superior visible-light-driven photocatalyst for hydrogen evolution, Appl. Catal., B 321 (2023) 122028.

[20] M. Tan, Y. Ma, C. Yu, Q. Luan, J. Li, C. Liu, W. Dong, Y. Su, L. Qiao, L. Gao, Boosting photocatalytic hydrogen production via interfacial engineering on 2D ultrathin Z-scheme $ZnIn_2S_4$/g-C_3N_4 heterojunction, Adv. Funct. Mater. 32 (2022) 2111740.

[21] S. Sun, Y.C. Zhang, G. Shen, Y. Wang, X. Liu, Z. Duan, L. Pan, X. Zhang, J.J. Zou, Photoinduced composite of Pt decorated Ni $(OH)_2$ as strongly synergetic cocatalyst to boost H_2O activation for photocatalytic overall water splitting, Appl. Catal., B 243 (2019) 253–261.

[22] B. Zhou, Y. Li, Y. Zou, W. Chen, W. Zhou, M. Song, Y. Wu, Y. Lu, J. Liu, Y. Platinum modulates redox properties and 5-hydroxymethylfurfural adsorption kinetics of Ni$(OH)_2$ for biomass upgrading Wang, Angew. Chem., Int. Ed. 60 (2021) 22908–22914.

[23] Z. Zhao, X. Diao, P. Wang, H. Gao, J.T. Irvine, R. Liu, X. Zhang, G. Wang, Assembling ultrathin nickel hydroxide nanosheets on cadmium sulfide hollow spheres for enhanced CO_2 photoreduction, J. Chem. Eng. 482 (2024) 149184.

[24] H. Zhao, Z. Jiang, K. Xiao, H. Sun, H.S. Chan, T.H. Tsang, S. Yang, P.K. Wong, Photo-assisted separation of noble-metal-free oxidation and reduction cocatalysts for graphitic carbon nitride nanosheets with efficient photocatalytic hydrogen evolution, Appl. Catal., B 280 (2021) 119456.

[25] M. Humayun, C. Wang, W. Luo, Recent progress in the synthesis and applications of composite photocatalysts: a critical review, Small Methods 6 (2022) 2101395.

[26] G. Li, Z. Lian, Z. Wan, Z. Liu, J. Qian, Y. Deng, S. Zhang, Q. Zhong, Ni $(OH)_2$ clusters decorated $NiTiO_3$ Z-scheme heterojunctions with strong O_2 activation and robust interfacial built-in electric field for efficient NO photo-oxidation, J. Chem. Eng. 451 (2023) 138625.

[27] J. Lin, W. Tian, H. Zhang, H. Sun, S. Wang, Electronic structure and functions of carbon nitride in frontier green catalysis, Acc. Chem. Res. 57 (2024) 2303–2315.

[28] X. Ruan, S. Li, C. Huang, W. Zheng, X. Cui, S.K. Ravi, Catalyzing artificial photosynthesis with TiO_2 heterostructures and hybrids: emerging trends in a classical yet contemporary photocatalyst, Adv. Mater. 36 (2024) 2305285.

[29] Y. Jiang, H. Sun, J. Guo, Y. Liang, P. Qin, Y. Yang, L. Luo, L. Leng, X. Gong, Z. Wu, Vacancy engineering in 2D transition metal chalcogenide photocatalyst: structure modulation, function and synergy application, Small 20 (2024) 2310396.

[30] W. Jiang, R. Li, J. He, S. Ni, L. Wang, Z. Chen, Y. Huang, C. Li, J. Yi, M. Song, Nitrogen-doping assisted local chemical heterogeneity and mechanical properties in CoCrMoW alloys manufactured via laser powder bed fusion, Adv. Powder Mater. 3 (2024) 100217.

[31] F. Wu, X. Zhang, L. Wang, G. Li, J. Huang, A. Song, A. Meng, Z. Li, Enhanced spin-polarized electric field modulating p-band center on Ni-doped CdS for boosting photocatalytic hydrogen evolution, Small 20 (2024) 2309439.

[32] H. Liao, K. Huang, W. Hou, H. Guo, C. Lian, J. Zhang, Z. Liu, L. Wang, Atmosphere engineering of metal-free Te/C_3N_4 pn heterojunction for nearly 100% photocatalytic converting CO_2 to CO, Adv. Powder Materials 3 (2024) 100243.

[33] J. Ni, R. Zhao, C. Shi, Y. Ji, A. Hao, A. Xie, H. Yu, S.K. Boong, H.K. Lee, C. Zhou, Structure-tailored superlattice $Bi_7Ti_4NbO_{21}$: coupling octahedral tilting and rotation induced high ferroelectric polarization for efficient piezo-photocatalytic CO_2 reduction, Adv. Powder Mater. (2025) 100265.

[34] F. Wang, C. Hu, C. Chen, S. Cao, Q. Li, Y. Wang, J. Ma, Enhanced photocatalytic water splitting over nickel-doped CdS nanocomposites synthesized via one-step controllable irradiation routine at ambient conditions, Appl. Surf. Sci. 614 (2023) 156190.

[35] M. Li, F. Chen, Y. Xu, M. Tian, Ni $(OH)_2$ nanosheet as an efficient cocatalyst for improved photocatalytic hydrogen evolution over $Cd_{0.9}Zn_{0.1}S$ nanorods under visible light, Langmuir 40 (2024) 3793–3803.

[36] T. Zhu, Y. Liang, Y. Wang, J. Wang, W. Wang, J. Fu, L. Yao, Y. Cheng, H. Han, P-type β-Ni $(OH)_2$ nanoparticles sensitize CdS nanorod array photoanode to prolong charge carrier lifetime and highly improve bias-free visible-light-driven H_2 evaluation, Appl. Catal., B 271 (2020) 118945.

[37] Y. Chen, T. Shan, L. Liu, L. Shen, H. Xue, M.Q. Yang, Construction of embedded CdS nanosheets@PEA_2PbBr_4 nanoplate p-n heterojunction photocatalysts with spatial charge transfer for enhanced benzylic C (sp3)-H bond oxidation, J. Chem. Eng. 480 (2024) 148099.

[38] B. He, P. Xiao, S. Wan, J. Zhang, T. Chen, L. Zhang, J. Yu, Rapid charge transfer endowed by interfacial Ni–O bonding in S-scheme heterojunction for efficient photocatalytic H_2 and imine production, Angew. Chem. Int. Ed. 62 (2023) 202313172.

[39] Y. Ai, J. Hu, X. Xiong, S.A. Carabineiro, Y. Li, N. Sirotkin, A. Agafonov, K. Lv, Synergistic interfacial engineering of a S-scheme ZnO/In_2S_3 photocatalyst with S–O covalent bonds: a dual-functional advancement for tetracycline hydrochloride degradation and H_2 evolution, Appl. Catal., B 353 (2024) 124098.

[40] Z. Fan, Y. Cai, Z. Yang, X. Zhang, R. Shao, S. Zhong, L. Zhao, D. Liu, S. Bai, Integrating CO_2 reduction, H_2O oxidation and H_2 evolution catalysts into a dual S-scheme artificial photosynthetic system for tunable syngas production, Appl. Catal., B 351 (2024) 123979.

[41] M. Liu, W. Yang, R. Xiao, Y. Qin, R. Tan, Y. Chen, W. Gu, L. Hu, Y. Lin, C. Zhu, Anisotropic dual S-scheme heterojunctions mimic natural photosynthetic system for boosting photoelectric response, Angew. Chem. Int. Ed. 136 (2024) 202407481.

[42] L. Wu, S. Zheng, H. Lin, S. Zhou, A.M. Idris, J. Wang, S. Li, Z. Li, In-situ assembling 0D/2D Z-scheme heterojunction of lead-free $Cs_2AgBiBr_6/Bi_2WO_6$ for enhanced photocatalytic CO_2 reduction, J. Colloid Interface Sci. 629 (2023) 233–242.

[43] J. Liu, E. Jia, L. Wang, K.A. Stoerzinger, H. Zhou, C.S. Tang, X. Yin, X. He, E. Bousquet, M.E. Bowden, Tuning the electronic structure of $LaNiO_3$ through alloying with strontium to enhance oxygen evolution activity, Adv. Sci. 6 (2019) 1901073.

[44] Z. Feng, F. Lu, Q. Hu, J. Qiu, X. Lei, B. Wang, R. Guo, Y. Tian, X. Liu, J. You, Built-in electric fields and extra electric fields in the oxygen evolution reaction, J. Mater. Chem. A 12 (2024) 18047–18070.

[45] I.A. Digdaya, G.W. Adhyaksa, B.J. Trześniewski, E.C. Garnett, W.A. Smith, Interfacial engineering of metal-insulator-semiconductor junctions for efficient and stable photoelectrochemical water oxidation, Nat. Commun. 8 (2017) 15968.

[46] I. Vamvasakis, I.T. Papadas, T. Tzanoudakis, C. Drivas, S.A. Choulis, S. Kennou, G.S. Armatas, Visible-light photocatalytic H_2 production activity of β-Ni$(OH)_2$-modified CdS mesoporous nanoheterojunction networks, ACS Catal. 8 (2018) 8726–8738.

[47] A.M. Idris, S. Zheng, L. Wu, S. Zhou, H. Lin, Z. Chen, L. Xu, J. Wang, Z. Li, A heterostructure of halide and oxide double perovskites $Cs_2AgBiBr_6/Sr_2FeNbO_6$ for boosting the charge separation toward high efficient photocatalytic CO_2 reduction under visible-light irradiation, J. Chem. Eng. 446 (2022) 137197.

[48] J. Fu, Q. Xu, J. Low, C. Jiang, J. Yu, Ultrathin 2D/2D WO_3/g-C_3N_4 step-scheme H_2-production photocatalyst, Appl. Catal., B 243 (2019) 556–565.

[49] Y. Jiang, H.Y. Chen, J.Y. Li, J.F. Liao, H.H. Zhang, X.D. Wang, D.B. Kuang, Z-scheme 2D/2D heterojunction of $CsPbBr_3/Bi_2WO_6$ for improved photocatalytic CO_2 reduction, Adv. Funct. Mater. 30 (2020) 2004293.

[50] X. Wang, Z. Wang, Y. Li, J. Wang, G. Zhang, Efficient photocatalytic CO_2 conversion over 2D/2D Ni-doped $CsPbBr_3/Bi_3O_4Br$ Z-scheme heterojunction: critical role of Ni doping, boosted charge separation and mechanism study, Appl. Catal., B 319 (2022) 121895.

[51] M. Zhang, Y. Mao, X. Bao, G. Zhai, D. Xiao, D. Liu, P. Wang, H. Cheng, Y. Liu, Z. Zheng, Y. Dai, Y. Fan, Z. Wang, B. Huang, Coupling benzylamine oxidation with CO_2 photoconversion to ethanol over a black phosphorus and bismuth tungstate S-Scheme heterojunction, Angew. Chem. Int. Ed. 62 (2023) 202302919.

[52] Y. Deng, C. Wan, C. Li, Y. Wang, X. Mu, W. Liu, Y. Huang, P.K. Wong, L. Ye, Synergy effect between facet and zero-valent copper for selectivity photocatalytic methane formation from CO_2, ACS Catal. 12 (2022) 4526–4533.

[53] X. Ren, M. Gao, Y. Zhang, Z. Zhang, X. Cao, B. Wang, X. Wang, Photocatalytic reduction of CO_2 on BiO_x, effect of halogen element type and surface oxygen vacancy mediated mechanism, Appl. Catal., B 274 (2020) 119063.

[54] X. Zu, Y. Zhao, X. Li, R. Chen, W. Shao, L. Li, P. Qiao, W. Yan, Y. Pan, Q. Xu, J. Zhu, Y. Sun, Y. Xie, Reversible switching Cu II/Cu I single sites catalyze high-rate and selective CO_2 photoreduction, Angew. Chem. Int. Ed. 62 (2022) 202215247.

[55] K. Zhang, H. Chen, Y. Liu, J. Deng, L. Jing, A. Rastegar Panah, W. Pei, Z. Han, H. Dai, Two-dimensional $Bi_2W_xMo_{1-x}O_6$ solid solution nanosheets for enhanced photocatalytic toluene oxidation to benzaldehyde, Appl. Catal., B 315 (2022) 121545.
[56] S. Zhu, B. Jiang, W.B. Cai, M. Shao, Direct observation on reaction intermediates and the role of bicarbonate anions in CO_2 electrochemical reduction reaction on Cu surfaces, J. Am. Chem. Soc. 139 (2017) 15664–15667.
[57] Z. Miao, Q. Wang, Y. Zhang, L. Meng, X. Wang, In-situ construction of S-scheme AgBr/BiOBr heterojunction with surface oxygen vacancy for boosting photocatalytic CO_2 reduction with H_2O, Appl. Catal., B 301 (2022) 120802.
[58] D. Zhou, X. Xue, X. Wang, Q. Luan, A. Li, L. Zhang, B. Li, W. Dong, G. Wang, C. Hou, Ni, in co-doped $ZnIn_2S_4$ for efficient hydrogen evolution: modulating charge flow and balancing H adsorption/desorption, Appl. Catal., B 310 (2022) 121337.
[59] E.R. Sauve, B.Y. Tang, N.K. Razdan, W.L. Toh, S. Weng, Y. Surendranath, Open circuit potential decay transients quantify interfacial pH swings during high current density hydrogen electrocatalysis, Joule 8 (2024) 728–745.
[60] K. Khan, L. Xu, M. Shi, J. Qu, X. Tao, Z. Feng, C. Li, R. Li, Surface assembly of cobalt species for simultaneous acceleration of interfacial charge separation and catalytic reactions on $Cd_{0.9}Zn_{0.1}S$ photocatalyst, Chinese, J. Catal. 42 (2021) 1004–1012.
[61] B. Wang, S. He, L. Zhang, X. Huang, F. Gao, W. Feng, P. Liu, CdS nanorods decorated with inexpensive NiCd bimetallic nanoparticles as efficient photocatalysts for visible-light-driven photocatalytic hydrogen evolution, Appl. Catal., B 243 (2019) 229–235.
[62] J. Wang, T. Xia, L. Wang, X. Zheng, Z. Qi, C. Gao, J. Zhu, Z. Li, H. Xu, Y. Xiong, Enabling visible-light-driven selective CO_2 reduction by doping quantum dots: trapping electrons and suppressing H_2 evolution, Angew. Chem. Int. Ed. 57 (2018) 16447–16451.
[63] Z. Zhao, X. Diao, P. Wang, H. Gao, J.T. Irvine, R. Liu, X. Zhang, G. Wang, Assembling ultrathin nickel hydroxide nanosheets on cadmium sulfide hollow spheres for enhanced CO_2 photoreduction, J. Chem. Eng. 482 (2024) 149184.

Dr. Khakemin Khan obtained a Ph.D. in 2021 from the Dalian Institute of Chemical Physics, specializing in photocatalysis. Currently, Dr. Khakemin Khan is working as a postdoctoral researcher at the Physics Department of Trento University, Italy. Currently, his major research interests are focused on the design and fabrication of integrated nanocatalysts for energy conversion and storage.

Ahmed Mahmoud Idris received his Ph.D. degree from the Dalian Institute of Chemical Physics, Chinese Academy of Sciences, in 2021. From 2021 to 2022, he conducted postdoctoral research at Zhejiang Normal University, Jinhua, Zhejiang, China. In 2023, he works as a research professor at the School of Physics and Electronic Information Engineering, Zhejiang Normal University. His research interests include the design and synthesis of nanomaterials, interfacial engineering for photo(electro)catalysis in energy conversion and storage.

Prof. Antonio Miotello graduated in physics at University of Padova and after obtaining the position of professor of experimental Physics he moved to the University of Trento at the Department of Physics. Here he was also director of the department and head of “IdEA (Hydrogen, Energy, Environment)” laboratory dedicated to material science for production of new materials relevant in the energy and environmental fields. The research activity has also allowed the development of patents for applications in the field of solar concentration and coating of materials operating in extreme pressure and temperature conditions (acquired by the industry).